Energy Storage Materials 53 (2022) 212–221

Contents lists available at ScienceDirect

Energy Storage Materials

journal homepage: www.elsevier.com/locate/ensm

In situ mitigating cation mixing of Ni-rich cathode at high voltage via Li_2MnO_3 injection

Binhong Wu [a], Zhiye Lin [a], Gaige Zhang [a], Dehui Zhang [a], Wenguang Zhang [a], Guanjie Li [a], Yanxia Che [a], Ling Chen [a], Huirong Wang [a], Weishan Li [a,b], Min Chen [a,b,*], Guozhong Cao [c,*]

[a] School of Chemistry, South China Normal University, Guangzhou 510006, China
[b] Engineering Research Center of MTEES (Ministry of Education), Research Center of BMET (Guangdong Province), Engineering Lab. of OFMHEB (Guangdong Province), Key Lab. of ETESPG (GHEI), Innovative Platform for ITBMD (Guangzhou Municipality), South China Normal University, Guangzhou 510006, China
[c] Department of Materials Science and Engineering, University of Washington, Seattle WA 98195, United States

ARTICLE INFO

Keywords:
Lithium-ion batteries
Ni-rich cathode
Cation mixing
Li_2MnO_3
Lithium voids

ABSTRACT

Ni-rich layered oxides ($LiNi_xCo_yMn_zO_2$, $x \geq 0.8$) have been under intense investigation as cathode materials for high-energy rechargeable lithium ion batteries (LIBs) due to their high capacity and relatively low cost. However, Ni/Li cation mixing, in most cases, brings about capacity degradation, structure evolution and poor thermal stability, especially at high cut-off voltage. Herein, a universal strategy with novel mechanism-*in situ* mitigating cation mixing at 4.55 V via injecting Li_2MnO_3 has been achieved (label as LD-NCM811), significantly improving the electrochemical property, structural integrity and thermal stability of Ni-rich cathode materials compared with the conventional NCM811. LD-NCM811 maintains a high capacity retention of 93% at 0.3 C after 200 cycles at 25 °C with negligible voltage decay of 40 mV, whereas the NCM811 shows a retention of 68% and large voltage decay of 248 mV, and the corresponding cation mixing has been mitigated from 13.5% to 7.5%. At the temperature of 45 °C, LD-NCM811 still keeps a considerable capacity retention of 93% at 1 C, significantly superior to the NCM811 with 75%. Characterization and calculation reveal that the excellent performances result from the Li_2MnO_3 phase with unique superlattice providing lithium voids in transition metal (TM) oxide layers when it is charged above 4.5 V, which is favorable for the mixed Ni ions migrating back to TM layers instead of blocking the lithium channel. This new finding establishes a general strategy for mitigating cation mixing of NCM811 to realize its application in high energy density and safety batteries.

1. Introduction

With the development of our society, the demand for energy is also increasing rapidly, especially vehicles, which causes the consumption of fossil energy soaring to the top, resulting in environment contamination. Due to the characteristics of high energy density, long cycle life and zero-emission, lithium-ion batteries (LIBs) have been considered as the most promising renewable power source for portable electronic devices and even pure electric vehicles [1,2]. However, the commercial $LiCoO_2$/graphite cell cannot meet the demands for higher energy density batteries with long-miles and low cost [3,4]. Therefore, many alternative cathode materials have been developed, such as $LiFePO_4$ [5], $LiMn_2O_4$ [6], and Ni-rich layered oxides ($LiNi_xCo_yAl_zO_2$, NCA; $LiNi_xCo_yMn_zO_2$, NCM, x>0.8, x+y+z=1) [7]. Among them, Ni-rich layered oxides have attracted much attention because of their large capacity, high working voltages (about 3.8 V vs. Li^+/Li) and low cobalt consumption. [8,9] For example, the currently developed cell for Tesla EVs (models S, X, and 3) based on a Ni-rich NCA cathode have been commercialized [10]. However, the current state-of-the-art NCA applied for EVs is insufficient for safety assurance [11,12]. Thus, the more thermal stable NCM has been regarded as the alternate cathode for EVs.

As for Ni-rich NCM, their capacity is increasing with the increase of Ni content and the cut-off voltage. For the sake of improving the energy density of Ni-rich NCM battery, one efficient way is to increase the cut-off voltage. While the structural evolution from layered over spinel to NiO-like rock-salt phase and thermodynamic instability caused by Li/Ni cation mixing seriously limits their developments under high voltage. In order to suppress cation mixing of Ni-rich NCM, tremendous strategies have been investigated, such as surface coating, cation/anion doping, single crystal construction and even compositional gradients [13–24].

* Corresponding authors.
E-mail addresses: chenmin@m.scnu.edu.cn (M. Chen), gzcao@u.washington.edu (G. Cao).

https://doi.org/10.1016/j.ensm.2022.09.008
Received 9 June 2022; Received in revised form 28 August 2022; Accepted 11 September 2022
Available online 13 September 2022

As for the first one, it protects the deeply delithiated cathode from parasitic reaction with electrolyte, while cation/anion doping stabilizes the layer structure via pillar effect, developing single crystal structure reduces the grain boundary, and the last one utilizes more Mn^{4+} near the particle surface and Ni^{3+} in the core to reduce interface side reaction. For example, Sun et al. introduced Li $[Ni_{0.5}Mn_{0.5}]O_2$ shell to protect NCM811 and improve the cycle stability, but the coating layer with heterogeneous anisotropic strain could not effectively prevent subsequent capacity fading [13]. Xie et al. doped Mg^{2+} in Li sites to enhance the thermal stability and rate capability of NCM811, and Weigel et al. doped Zr^{4+} in Ni sites to mitigate the releasing of O_2 at the fully delithiated state, but the delivery capacity of them was sacrificed [16,17]. Ryu et al. reported a series of single-crystal, Ni-rich Li $[Ni_xCo_yMn_{1-x-y}]O_2$ (NCM) to resist mechanical microcracking while they exhibit sluggish kinetics due to longer channel for Li^+ to transport [23]. Park et al. synthesized a full concentration gradient (FCG) lithium transition-metal oxide particle where nickel concentration decreases from the center towards the outer layer and the concentration of manganese increases accordingly to enhance the thermal stability and electrochemical performance, but such concentration distribution is difficult to control [14]. However, all the methods mitigate cation mixing through a static process, which means that they just suppress the migration of Ni ions from the TM layers to lithium layers via heteroatom occupation but cannot provide remaining voids in TM layers to let the Ni ions return freely.

In this work, a universal strategy of *in situ* suppressing cation mixing during cycling is achieved by injecting 2.38% Li_2MnO_3 into NCM811 (LD-NCM811). Electrochemical results show that LD-NCM811 has a high capacity retention of 93% at 0.3 C after 200 cycles at 25 °C with negligible voltage decay of 40 mV, whereas the NCM811 suffers from a retention of 68% and large voltage decay of 248 mV. Even at 45 °C, LD-NCM811 keeps a high capacity retention of 93% at 1 C after 100 cycles while only 75% capacity retention for NCM811. *Ex-situ* X-ray diffraction (XRD) demonstrates that the cation mixing of NCM811 is mitigated from 13.5% to 7.5%, and the corresponding surface transition layer is largely suppressed in LD-NCM811. The improved performance can be explained by the fact that when the LD-NCM811 electrode is charged above 4.5 V, Li^+ deintercalate from Li_2MnO_3 and remain lithium voids in TM layer. In the subsequent charging process, the Ni ions occupied in lithium layers will spontaneously migrate to the formed lithium voids and back to TM layers, which reduces the amount of Ni ions in lithium layers and *in-situ* suppresses Li/Ni mixing and phase transformation.

2. Experimental section

2.1. Material synthesis

Spherical $[Ni_{0.776}Co_{0.097}Mn_{0.117}](OH)_2$ hydroxide precursors are synthesized via co-precipitation method. $NiSO_4{\cdot}6H_2O$, $CoSO_4{\cdot}7H_2O$ and $MnSO_4{\cdot}H_2O$ are used as raw materials at the molar ratio of 392:49:59 and dissolved in distilled water to form 1 M mixed solution. The buffer solution with pH 11 is obtained by mixing $NH_3{\cdot}H_2O$ and $(NH_4)_2SO_4$ solution at appropriate molar ratio. Then, the buffer solution is heated at 55 °C in water bath kettle, and stirred at a certain speed under N_2 atmosphere. Afterward, the mixed metal ions solution (1 M) and NaOH solution (2 M) are simultaneously added into the buffer solution at the same speed via a peristaltic pump. After completing the reaction, the precipitated product is collected and washed with distilled water for several times. Finally, the precursor powder $[Ni_{0.776}Co_{0.097}Mn_{0.117}](OH)_2$ is obtained after being dried at 120 °C for 12 h in a vacuum box. Precursor powder is mixed with $LiOH{\cdot}H_2O$ at the appropriate molar ratio of Li/(Ni+Co+Mn), which is 1.02 / 1 for $[Ni_{0.776}Co_{0.097}Mn0_{.117}](OH)_2$. Additionally, Li excess of 5 mol% is added to compensate for the evaporation of Li salt under high temperature. Then, the mixture is sintered at 500 and 800 °C in an O_2 flow for 5 and 12 h to get LD-NCM811. HLD-NCM811 and NCM811 are obtained in the same step only change the ratio of raw materials.

2.2. Materials characterization

The morphological images of pristine and cycled electrodes were acquired by scanning electron microscopy (SEM, FEI-quanta 250). The high-resolution transmission electron microscopy (HRTEM) and fast Fourier transformation (FFT) of lattice structure for pristine and cycled electrodes were acquired by transmission electron microscopy (TEM FEI-Talos F200X). The scanning transmission electron microscopy (STEM) images were recorded by a FEI Cs-corrected Titan microscope (FEI Titan Cubed Themis G2). XRD (Rigaku Ultima IV, Japan) of the electrodes were obtained using monochromatic Cu Kα radiation between 10 and 100° at a scanning rate of 5° min^{-1}. Rietveld refinements of the XRD patterns were obtained by Fullprof. The thermal stability of cycled NCM811 and LD-NCM811 cathodes was evaluated by differential scanning calorimetry (DSC, TA-60WS, Japan) in a heating range from 30 to 300 °C at a heating rate of 10 °C min^{-1}. X-ray photoelectron spectroscopy (XPS, ESCALAB 250) was adopted to analyze the surface composition of pristine and cycled electrodes. The extended X-ray absorption fine structure (EXAFS) measurements were carried out on the sample at 21A X-ray nanodiffraction beamline of Taiwan Photon Source (TPS), National Synchrotron Radiation Research Center (NSRRC). This beamline adopted 4-bounce channel-cut Si (111) monochromator for mono-beam X-ray nanodiffraction and X-ray absorption spectroscopy. The end-station equipped with three ionization chambers and Lytle/SDD detector after the focusing position of KB mirror for transmission and fluorescence mode X-ray absorption spectroscopy. The photon flux on the sample is range from $1 \times 1011 \sim 3 \times 109$ photon/*sec* for X-ray energy from 6 to 27 keV.

2.3. Preparation of electrode and electrochemical measurements

A proportion of 80 wt% NCM811 and LD-NCM811 powders were adopted as the active materials, with 10 wt% acetylene black (Shenzhen Kejing Star Technology Co., Ltd.) as the conductive agent and 10 wt% poly(vinylidene fluoride) (PVDF, Shenzhen Kejing Star Technology Co., Ltd.) as the binder. The mixtures were blended in N-methyl pyrrolidone (NMP) solvent. After a period of stirring, the obtained slurries are coated onto the current aluminum foil collector. The electrodes are dried at 80 °C for 1 h and 120 °C for 12 h under vacuum conditions to completely remove the NMP solvent. Then, the dry electrodes are cut into circles with a diameter of 12 mm. The average mass loadings were about 2.0 mg cm^{-2} for all the cathode electrodes.

CR2025 coin-type half-cell and *in situ*-XRD simulative cell were assembled in an Ar-filled glove box (MBraun, Germany, O_2, H_2O <0.01 ppm) using lithium metal as the anode, polypropylene microporous film (Cellgard 2300) as separator, 1 M $LiPF_6$ in EC:DEC:EMC (3:2:5 in weight) as electrolyte at room temperature (25 °C). The amount of electrolyte used for each cell is 60 μl. The cycling and rate performance is carried on LAND CT2001A system (Wuhan Bartray Technology, China). The initial charge curve of NCM811 and LD-NCM811 was performed on *in situ* XRD simulative cell at 0.1 C with voltage window of 2.8–4.55 V. Electrochemical impedance spectroscopy (EIS) is obtained from PGSTAT-30 electrochemical station (Metrohm, Netherlands) with a frequency range from 10^5 to 0.01 Hz at the potential amplitude of 5 mV.

2.4. Calculation method

Density functional theory calculations (DFT) are performed using the projector-augmented wave method as implemented in the VASP code [25–27]. The plane-wave cutoff energy is set to 400 eV. For the exchange-correlation functional, the Perdew–Burke–Ernzerhof (PBE)2 generalized gradient approximation (GGA) is used to calculate energy. The calculation is carried out with a $2 \times 2 \times 1$ supercell of 108 atoms. For periodic calculations, Γ-centered k-meshes with k-spacing of 0.2 $Å^{-1}$ is employed. The atomic positions are optimized until residual forces on

each atom are less than 0.01 eV $Å^{-1}$.

3. Results and discussion

The XRD patterns and Rietveld refinements for pristine LD-NCM811 and NCM811 are shown in Fig. 1a, b. Both cathodes have a typical hexagonal α-$NaFeO_2$ layered structure with a space group of R-3 m. Obvious splitting of the (006)/(102) and (108)/(110) pairs reveals the prominent layer structure of both LD-NCM811 and NCM811 [28]. The XRD refinement results exhibit that the weight fraction of C2/m and R-3 m phase belonging to LD-NCM811 is 2.38% and 97.62%, respectively, indicating the successful injection of Li_2MnO_3 in NCM811. Lattice parameters of LD-NCM811 and NCM811 shown in Supplementary **Table S1** reveal that the parameter of c_{hex} of LD-NCM811 is larger than NCM811, indicating that Li_2MnO_3 has been injected into bulk NCM811 phase rather than enrichment on surface. Moreover, when compared with $LiMO_2$ phase, Li_2MnO_3 brings about excess Li ions in TM layers along *c* axis, which results in dilated c_{hex} due to its less charge and the expansion of cell volume in LD-NCM811. The enhanced c_{hex} is much easier for Li^+ insertion/de-insertion to improve the rate capability [29]. The *c*/*a* ratio of LD-NCM811 and NCM811 is 4.96 and 4.95, indicating that both samples have a good layered structure [30]. Atomic site occupation at the pristine state is calculated and presented in Supplementary **Tables S2–3**. 5% of cation mixing emerges in LD-NCM811, and 6% in NCM811, indicating that little cation mixing exists in both pristine samples. LD-NCM811 presents typical Raman hybrid vibration features

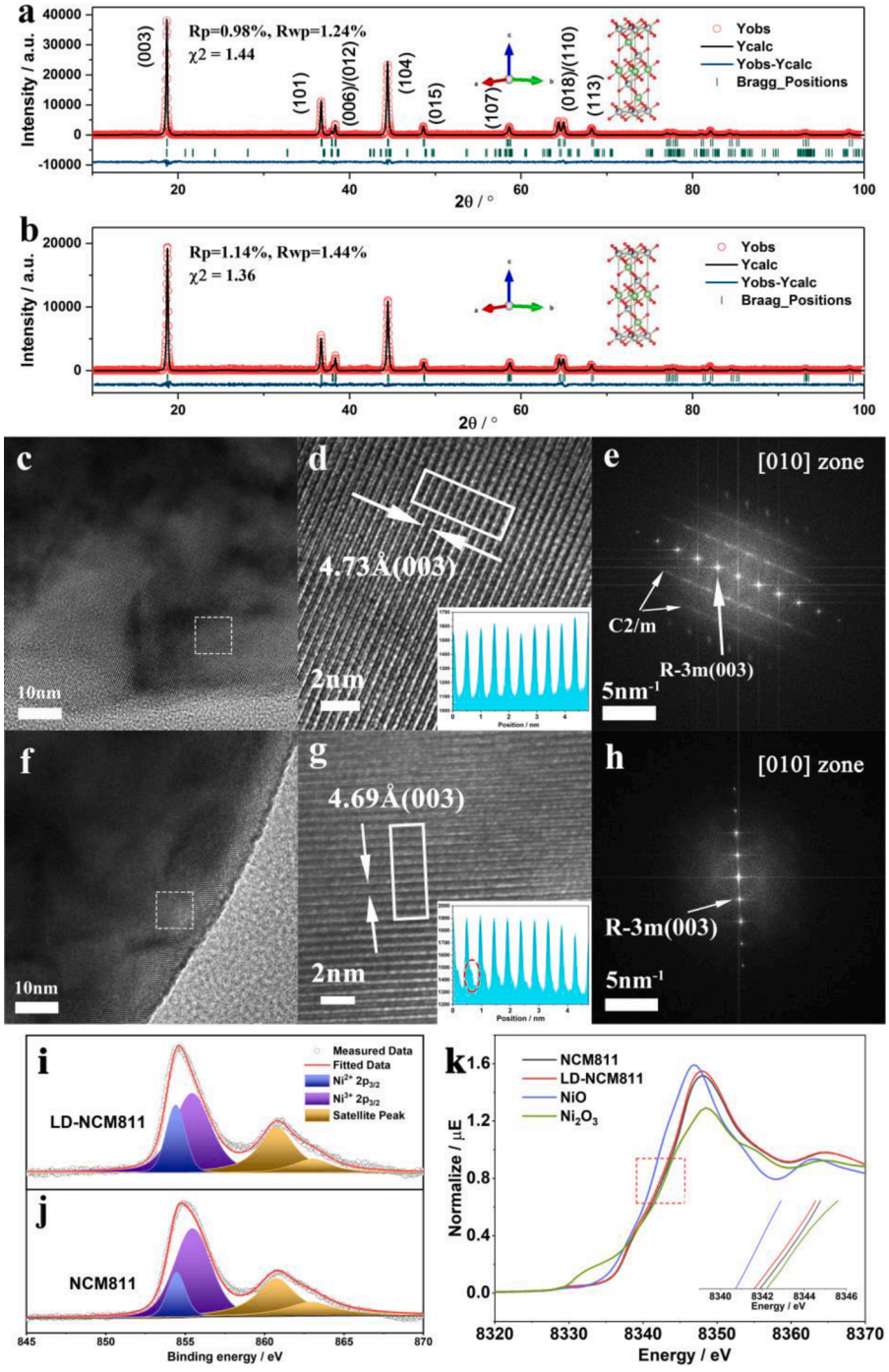

Fig. 1. XRD patterns and Rietveld refinements for pristine LD-NCM811(a) and NCM811(b); TEM images of LD-NCM811(c) and NCM811(f); HRTEM images of LD-NCM811(d) and NCM811(g) and their corresponding FFT images in [010] zone projection (e, h), the inset are their corresponding line profiles of the Z-contrast information with the measured spacing of TM layers. XPS spectra of LD-NCM811 (i) and NCM811 (j) at pristine state. Normalized Ni K-edge XANES spectra (k) of Ni in LD-NCM811 and NCM811 respectively.

of layered Li_2MnO_3 and $LiMO_2$. As shown in LD-NCM811 (Supplementary **Fig. S1**a), the peak positions of the blue region near 590 cm^{-1}, 490 cm^{-1} indicate A_{1g} (the TM-O stretching mode) and E_g (O-TM-O bending mode) vibrations of R-3 m structure respectively; the other three yellow regions around 380 cm^{-1}, 430 cm^{-1} and 530 cm^{-1} are assigned to the phonon vibrations of Li_2MnO_3. While NCM811 only exhibits A_{1g} and E_g vibration mode of $LiMO_2$, which also reveals that the successful injecting Li_2MnO_3 in NCM811 [31–33].

The morphologies of LD-NCM811 and NCM811 are presented by SEM images in Supplementary **Fig. S2** a, b. Both cathode materials contain spherically secondary particles approximately with a size of 8 μm, in which 300–600 nm sized primary particles are tightly packed. Supplementary **Fig. S3**a, b shows the TEM images of primary particles of LD-NCM811 and NCM811 respectively. The TEM images in Fig. 1c, f and their corresponding HRTEM images in Fig. 1d, g show clear lattice fringes, indicating the good crystalline structure with the well-defined layered structure for both samples [3]. The interplanar distance of the lattice planes is measured to be 4.73 Å and 4.69 Å for LD-NCM811 and NCM811, which is assigned to (003) facet [34,35]. The enlarged interplanar spacing of LD-NCM811 well agrees with XRD result, which also suggests Li_2MnO_3 phase has been stuck in $LiMO_2$ structure. As shown in the line profiles of the Z-contrast information (inset Fig. 1d, g), there are more TM ions (the red circle) in lithium layers indicating more Ni/Li cation mixing in NCM811 sample, which dovetailed nicely with the above XRD refinement results [36]. As presented in Fig. 1e, h, the FFT images of both LD-NCM811 and NCM811 are taken from the area (the same as HRTEM images) in [010] zone projection. Notably, besides the bright diffraction spots in the FFT image assigned to (003) facet in R-3 m structure, extra diffuse streaks also localize in LD-NCM811. Boulineau et al. reported that diffuse streaks is the signatures of the superlattice diffraction in Li_2MnO_3 with C2/m space group, where $Li_{1/3}(TM)_{2/3}$ slabs in TM layers [37]. The selected area electron diffraction (Supplementary **Fig. S4**b) originated from the aberration corrected TEM (Supplementary **Fig. S4**a) further confirmed the stacking faults with the existence of Li_2MnO_3. HAADF-STEM images of LD-NCM811 at edge and inner area along [100] zone axis are provided. From Supplementary **Fig. S4**c, it notes that several layers TM ions occupy in Li layer without Li_2MnO_3 phase aggregation. As can be seen from Supplementary **Fig. S4**d-f, there are randomly distributed hexagonal $LiMO_2$ (H) and monoclinic Li_2MnO_3 (M) and their disorder slabs (H+M), suggesting Li_2MnO_3 has been implanted into NCM811.

As shown in Fig. 1i, j, the XPS spectra of Ni $2p_{3/2}$ in both samples show that the oxidation states of Ni ions are mixed divalent/trivalent states, and one binding energy at around 854.4 eV corresponds to Ni^{2+},

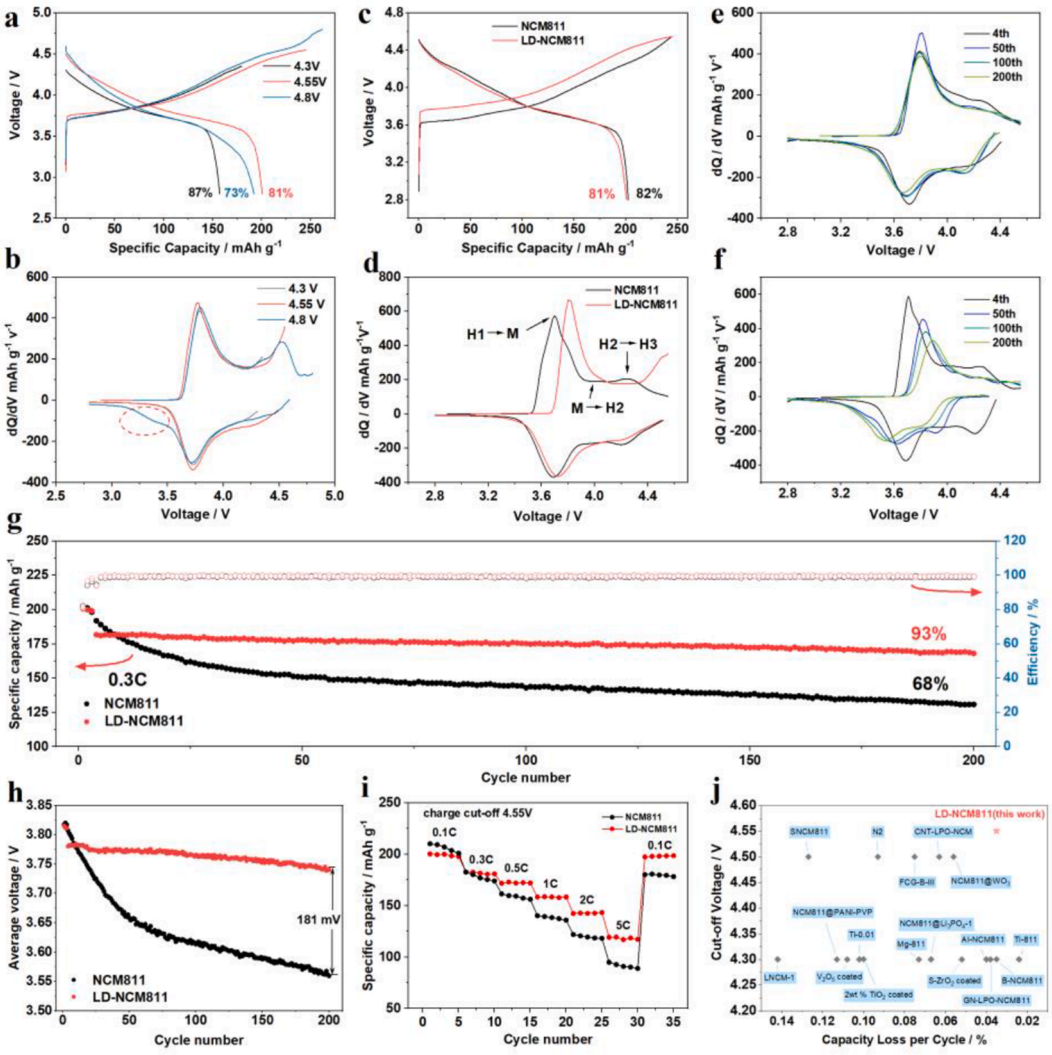

Fig. 2. The initial charge and discharge curves(a) and their corresponding dQ/dV curves(b) of LD-NCM811 at different cut-off voltage. The initial charge and discharge curves (c) and their corresponding dQ/dV curves (d) of NCM811 and LD-NCM811. dQ/dV curves of LD-NCM811 (e) and NCM811 (f) at different cycles. Cyclic stability (g) of NCM811 and LD-NCM811 at 0.3 C between 2.8 and 4.55 V. Curves of discharge medium voltage (h) of NCM811 and LD-NCM811. Rate performances (i) of NCM811 and LD-NCM811 electrodes. Comparison (j) of the electrochemical performance between this work and other modification works.

and another one at 855.5 eV is originated from Ni^{3+} [38]. Moreover, two satellite peaks of LD-NCM811 and NCM811 are observed around 860.7 eV and 863 eV, which is attributed to multiple splitting in the energy level of the Ni-containing oxides [38]. The normalized Ni K-edge X-ray absorption near edge structure (XANES) spectra of Ni in both samples (Fig. 1k) also support the XPS result. From the XPS fitting results, the ratio of $Ni^{2+}/(Ni^{2+}+Ni^{3+})$ in NCM811 is lower than that in LD-NCM811. XANES also reveals a subtle edge left shift of LD-NCM811 compared to NCM811. All the evidences combined suggests the introduction of Li_2MnO_3 in LD-NCM811 increases the amount of Mn^{4+} ions, resulting in more Ni^{2+} ions to maintain the charge balance.

The fundamental electrochemical performance of LD-NCM811 cathode is highly affected by the upper charge voltage due to the Li_2MnO_3 phase. Therefore, several cut-off voltages including 4.3 V, 4.55 V and 4.8 V are taken in the electrochemical test. As can be seen in Fig. 2a, LD-NCM811 delivers an initial discharge capacity of 169 mAh g^{-1}, 201 mAh g^{-1} and 192 mAh g^{-1} with Coulombic efficiencies of 87%, 81% and 73% at the voltage windows of 2.8–4.3 V, 2.8–4.55 V and 2.8–4.8 V respectively. dQ/dV curves (Fig. 2b) are plotted to understanding the redox of LD-NCM811 at different voltage. From the charging process, it is obvious that the cut-off voltage of 4.55 V involves partial activation of Li_2MnO_3, and 4.3 V does not activate the Li_2MnO_3-like component at all, whereas 4.8 V fully activates the Li_2MnO_3-like component. In the discharging process, fully activated Li_2MnO_3-like component displays a reduction peak below 3.5 V circled by the dash line, indicating the presence of redox reaction of Mn^{3+}/Mn^{4+} [3]. In general, Mn^{4+} in Ni-rich cathode does not participate redox reaction, but Mn^{4+}in LD-NCM811 undergoes redox between 2.8 and 4.8 V, which may result in Jahn-Teller effect in subsequent cycles [39]. However, scarcely any reduction peak is found below 3.5 V with a charge cut-off voltage of 4.55 V, which means hardly any Jahn-Teller effect happening between 2.8 and 4.55 V. Cycle performance of LD-NCM811 at three different cut-off voltages are shown in Supplementary **Fig. S5**. It reveals that LD-NCM811 delivers a considerably high capacity, the best cycling stability and the highest stable Coulombic efficiency between 2.8 and 4.55 V at 0.3 C when compared with other two voltage ranges. Accordingly, the charge cut-off voltage of 4.55 V is chosen in the subsequent studied and elaborated in the following discussion. The electrochemical performance of a high content of Li_2MnO_3 (3.61%) in NCM811 (HLD-NCM811) is also investigated. XRD patterns and Rietveld refinements for the pristine HLD-NCM811 are acquired and presented in Supplementary **Fig. S6** and Supplementary **Tables S4–5**. The electrochemical performances of HLD-NCM811 are displayed in Supplementary **Fig. S7**. According to Supplementary **Fig. S7**a, HLD-NCM811 delivers the lower initial discharge capacity of 192 mAh g^{-1} and exhibits inferior Colombic efficiency of 77%. HLD-NCM811 retains 91% capacity retention at 0.3 C after 200 cycles as shown in Supplementary **Fig. S7**b. 2.38% of Li_2MnO_3 appears to be the optimal content in this work, as less content cannot provide enough Li voids for nickel ions migrating to TM layers, and the following discussion is tested by LD-NCM811 and NCM811.

When comparing the initial charge-discharge curves (Fig. 2c) of the NCM811 and LD-NCM811 cathodes between 2.8 and 4.55 V at 0.1 C, the initial charge curve of LD-NCM811 shows not only a typical slope region but also a plateau region, and the former represents Li^+ de-insert from $LiMO_2$ and the latter corresponds Li^+ de-insert from Li_2MnO_3 [40,41]. The charge capacities of NCM811 and LD-NCM811 are 246 and 248 mAh g^{-1} with Coulombic efficiencies of 82% and 81%, respectively. The increasing charge capacity of LD-NCM811 may be explained by the fact that the partial activation of Li_2MnO_3. Their corresponding dQ/dV curves in Fig. 2d indicate the evolutions of different redox peaks. The redox peaks of both materials locate around 3.75 V, which corresponds to the redox of Ni^{2+}/Ni^{4+} and alternation of H1 and M phases [12,19]. The oxidation peak around 4.5 V of LD-NCM811 is the activation of Li_2MnO_3, accompanying Li^+ de-inserting from TM layers [42]. The cycle performance of LD-NCM811 and NCM811 are presented in Fig. 2g. The results show that the Coulombic efficiency of both materials is stable and close to 100%, NCM811 with more redox pair of Ni^{3+}/Ni^{4+} delivers a higher initial discharge capacity of 192 mAh g^{-1} at 0.3 C than LD-NCM811 (182 mAh g^{-1}), while LD-NCM811 delivers a stable discharge capacity with more excellent capacity retention of 93% after 200 cycles, compared with the only 68% in NCM811. The charge/discharge curves and corresponding dQ/dV plots of two samples are presented in Supplementary **Fig. S8**, and Fig. 2e, f. These results reveal that the charging platform rises and the oxidation peaks shift to the higher voltage, while the discharge platform descends and the reduction peaks shift to lower voltage, indicating the polarization increases during cycling. However, compared with NCM811, LD-NCM811 shows less shift and the reduction area, indicating less polarization and capacity decline. The curves of discharge medium voltage are presented in Fig. 2h. It can be seen from the curves that the voltage drop of LD-NCM811 is 40 mV after 200 cycles whereas NCM811 is 248 mV, which is nearly 6 times as the voltage drop of LD-NCM811. These results, illustrate that the voltage drop of LD-NCM811 is well depressed, contributed to the suppression of phase transformation driven by injecting Li_2MnO_3. Fig. 2i illustrates the excellent rate capacity of LD-NCM811. Although the initial capacity of LD-NCM811 is lower than NCM811, yet with the increasing rate from 0.1 C to 5 C, the capacity of LD-NCM811 retains much better than NCM811. In particular, the sample LD-NCM811 delivers the highest discharge capacity of 119 mA h g^{-1} at 5 C rate with capacity retention of 60%, which is much higher than 95 mAh g^{-1} for NCM811 with a capacity retention of 46%. Additionally, the discharge capacity of LD-NCM811 recovers to 198 mAh g^{-1} with capacity retention of 99% when the rate recovers to 0.1 C after high-rate cycling, whereas NCM811 is only 178 mAh g^{-1} with capacity retention of 86% (Supplementary **Fig. S9**). The poor rate capability of NCM811 is attributed to the degradation of the structure [43]. However, the excellent rate capability of LD-NCM811 is attributed to injecting Li_2MnO_3 in NCM811 to maintain the structural stability. Notably, the electrochemical properties and battery performances of LD-NCM811 are better than most samples that have been reported in open literature (Fig. 2j) [15,18,44–59].

The Nyquist plots all contain one or two semicircles and a slop line (Supplementary **Fig. S10** a, b), which can be well fitted by the equivalent circuit (Supplementary **Fig. S10** d). The small interception in the Z' axis corresponds to the Ohmic resistance of the cell (R_s), a semicircle at the high frequency represents the cathode electrolyte interface (CEI) film resistance (R_f) and a semicircle at medium frequency region is associated with charge transfer resistance (R_{ct}), the slope line in the low frequency region relates to Warburg impedance [60]. According to the fitting results, the simulated electrochemical parameters show that few differences of R_f are observed at 0.3 C during cycling. However, increasing rate of R_{ct} between LD-NCM811 and NCM811 becomes divergent (Supplementary **Fig. S10** c). At the 4th cycle, R_{ct} of LD-NCM811 and NCM811 is 111 Ω and 88 Ω respectively. When the cycle number turns to 50, R_{ct} of LD-NCM811 becomes 254 Ω, and NCM811 rapidly increases to 1744 Ω. The same trend appears at the 100th and 200th cycle for both materials. The R_{ct} value of LD-NCM811 is 422 Ω and 543 Ω respectively, in contrast to 2742 Ω and 3573 Ω of NCM811. The mitigated increase in R_{ct} of LD-NCM811 greatly suppresses the kinetic barrier for reversible lithium extraction/insertion, thereby leading to depressing capacity degradation. [61]

Fig. 3a, f present the TEM images of LD-NCM811 and NCM811 after 200 cycles with white dash line to separate the layer structure and structural reconstruction layer (SRL). The thickness of SRL of LD-NCM811 is only 3–10 nm whereas NCM811 steeply increases to more than 25 nm. According to Fig. 3b, the bulk structure LD-NCM811 retains the same as the pristine with the interplanar spacing of 4.73 Å assigned to (003) crystal plane of R-3 m structure, and line profiles of the Z-contrast information with the measured spacing of TM layers inset also illustrates no obvious cation mixing. Bright diffraction spots presented in FFT images (Fig. 3c) assign to (003) crystal plane of R-3 m structure,

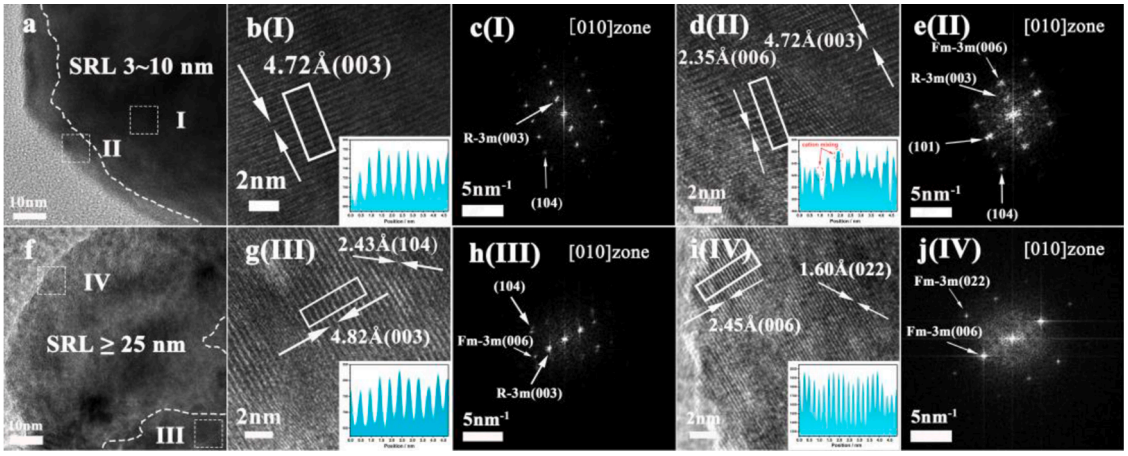

Fig. 3. Bright-field TEM images of LD-NCM811(a) and NCM811(f) after 200 cycles; HRTEM images with their line profiles of the Z-contrast images inset (b, g, d, i) and FFT images (c, h, e, j) of LD-NCM811(b-e) and NCM811(g-j). Fig. 3 (b, c) are from Fig. 3(a) region I; Fig. 3 (d, e) are from Fig. 3(a) region II; Fig. 3 (g, h) are from Fig. 3(f) region III; Fig. 3 (i, j) are from Figure (f) region IV.

well consisting with the corresponding HRTEM images. Fig. 3g shows the bulk HRTEM of NCM811 and the interplanar spacing of (003) increases to 4.82 Å. The enlarged interlayer distance indicates that the interaction between TM layers becomes weak as more Li^+ cannot go back. The bright diffraction lattice in FFT image (Fig. 3h) is corresponding to (003) facet of R-3 m group while the additional lattice is attributed to (006) space of Fm-3 m group [19,43]. This difference in bulk structure indicates two samples undergo different structure evolution. Moreover, surface region of both materials becomes more obvious. It can be seen from the HRTEM images (Fig. 3d) that a new crystal facet with an interplanar spacing of 2.35 Å emerges in LD-NCM811 and the corresponding FFT image (Fig. 3e) shows such face coexist with (003) crystal plane. The Z-contrast information with the measured spacing of TM layers also illustrates few TM ions existing in lithium layers. However, (006) crystal plane emerges and occupies the whole surface of NCM811 accompanied by disappearing of (003) crystal plane (Fig. 3i). Z-contrast information with the measured spacing of TM layers inset displays the interplanar spacing of 2.45 Å, indicating that the TM ions completely migrate to the lithium layers and generate a new crystal plane. Corresponding FFT image (Fig. 3j) distinctly presents the diffraction spots of (006) and (022) crystal planes, which indicates the migration of Ni^{2+} from TM layers to lithium layers and thicker Ni-O phase [19]. In addition, some lattice defects are observed from HRTEM image inset Fig. 3i, suggesting that NCM811 not only generates Ni-O phase but also suffers from structural damage at SRL, which is sufficiently severe to result in the development of a thick amorphous material on the particle surface. The HRTEM and FFT images of 4, 50 and 100 cycle numbers of LD-NCM811 and NCM811 presented in Supplementary **Fig. S11–13** also correspond to above discussions. Surprisingly, FFT images show that the diffuse streaks of C2/m structure in LD-NCM811 become weaker after 4 cycles. When the cycle number increases to 50, the diffuse streaks disappear, only to remain the diffraction spots of R-3 m structure. The same observation of 100 cycle numbers is shown in Supplementary **Fig. S13**. C2/m monoclinic structure of Li_2MnO_3 indicates excess Li^+ ordering in TM layers to form LiM_6 superlattice [62–65]. The gradually disappearing of C2/m structure indicates that the arrayed Li ions and superlattice structure in TM layers gradually disappear. This can be explained by the fact that the lithium voids in TM layers are occupied by Ni^{2+} ions migrating from lithium layers. This process, indicates that the process of mitigating cation maxing happens via Ni^{2+} ions migrating back to TM layers.

The XRD patterns and Rietveld refinements for LD-NCM811 and NCM811 after 100 cycles are presented in Supplementary **Fig. S14**. Both samples retain the most peaks of the pristine ones, but the relative peak intensity has been reduced, especially (003) peak of NCM811, revealing NCM811 with more serious structure damages. Lattice parameters of them shown in Supplementary **Table S8** reveal that the parameter of c_{hex} and volume (V) in NCM811 increases 0.71% and 0.62%, whereas LD-NCM811 only dilates 0.30% and 0.37%, suggesting that injecting Li_2MnO_3 effectively suppresses phase transition [66]. Atomic site occupation (Supplementary **Table S9, S10**) further illustrates that the extent of Li/Ni mixing in LD-NCM811 and NCM811 is 7.5% and 13.5% respectively, showing the mitigation of cation mixing in NCM811 via injecting Li_2MnO_3. XRD patterns of both materials at different cycles also confirm what we mentioned above (Supplementary **Fig. S15**). According to the TEM and XRD characterizations at different cycles, it is clear that with the increasing cycle number, cation mixing and phase transformation are severer, which not only blocks the lithium channel but also increases the R_{ct} and decreases the mass of active material, resulting in capacity and voltage fade, but injecting Li_2MnO_3 can mitigate such problems.

According to above results, the SRL is consisted of Ni-O phase, suggesting that the surface of materials is clustered with Ni^{2+} ions, as confirmed by following in-depth XPS [43,67,68]. From XPS fitting results in Supplementary **Fig. S16**, the ratio of $Ni^{2+}/(Ni^{2+}+Ni^{3+})$ via peak area was measured to quantitatively analysis the extent of cation mixing and phase transformation. It also can be seen from Fig. 4 that the relative proportion of peak area of $Ni^{2+}/(Ni^{2+}+Ni^{3+})$ of LD-NCM811 is lower than NCM811 after 100 cycles, and the ratio of $Ni^{2+}/(Ni^{2+}+Ni^{3+})$ of NCM811 and LD-NCM811 at surface is 61.3% and 39.0% respectively. Compared with the pristine state, the complicated evolution of the Ni $2p_{3/2}$ core spectra during cycling is caused by the multiple splitting of the energy levels of nickel oxides, verifying that nickel ions are the main components related to charge/discharge process and phase transformation [69]. As presented in Fig. 4, the main photo peaks at 852−860 eV correspond to Ni^{2+} and Ni^{3+} [69] After 100 cycles, the peaks at approximately 849 eV and 861 eV are commonly assigned as a satellite peak of nickel oxides. As sputtering time increasing, the ratio of $Ni^{2+}/(Ni^{2+} + Ni^{3+})$ dwindles, suggesting that the Ni-O phase SRL constitutes from bulk to surface. Moreover, the results obtained from the preliminary analysis of sputtering XPS spectra show that the ratio of $Ni^{2+}/(Ni^{2+} + Ni^{3+})$ of LD-NCM811 is 39%, 36.5%, 34.5% and 29.1% corresponding to the sputtering time of 0 s, 30 s, 60 s and 90 s respectively, whereas the ratio of $Ni^{2+}/(Ni^{2+} + Ni^{3+})$ of NCM811 is 61.3%, 51.1%, 49.2% and 45.5% respectively (Supplementary **Fig. S16**). As can be seen in these results, the constituent of Ni^{2+} in LD-NCM811 at the sputtering time of 90 s is approximate to its' pristine state, indicating that just mere material near the surface suffers from phase transformation. While the proportion of Ni^{2+} in NCM811 is 45.5%, which is much more than its' pristine state (19.9%), revealing that much of the

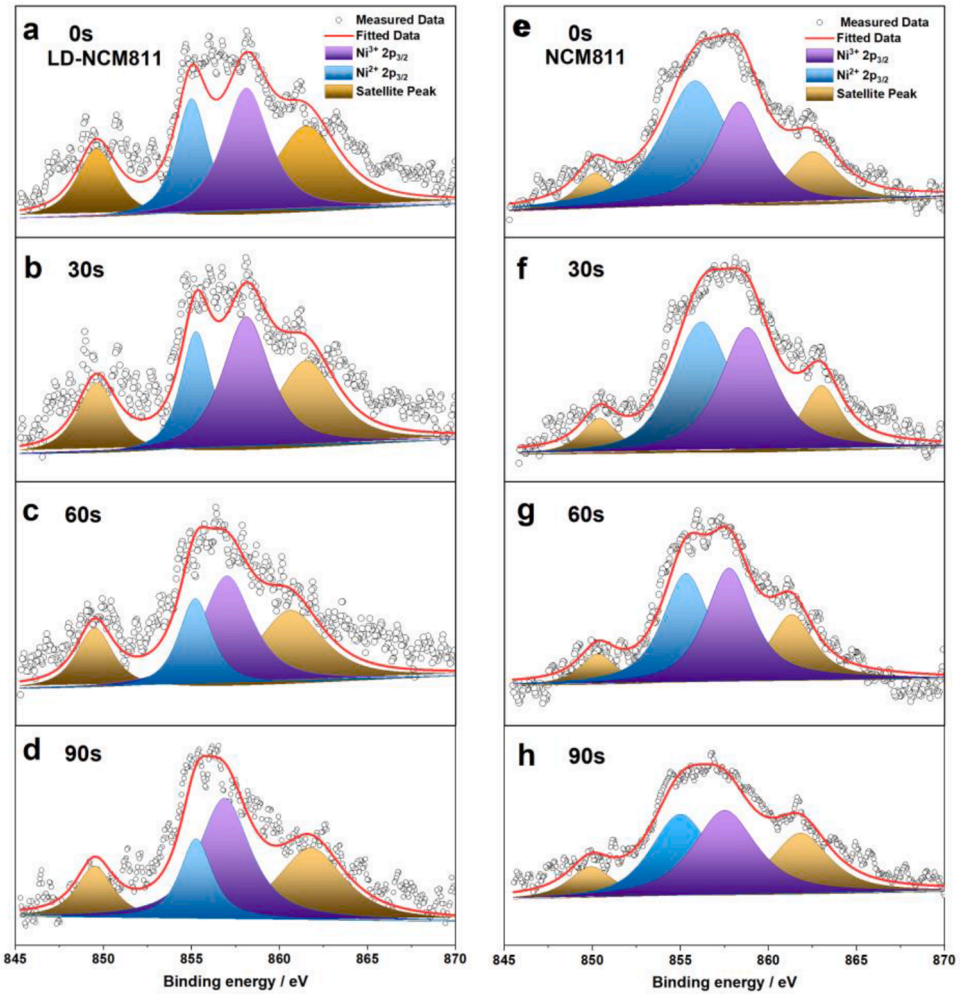

Fig. 4. XPS spectra of LD-NCM811 after 100 cycles at the sputtering time of 0 s (a), 30 s (b) 60 s (c) and 90 s (d). XPS spectra of NCM811 after 100 cycles at the sputtering time of 0 s (e), 30 s (f), 60 s (g) and 90s(h).

bulk structure undergoes phase transformation due to the cation mixing. Upon cycling, it can be seen that the area of Ni^{2+} of both materials is increasing and the area of Ni^{3+} is dwindling, suggesting that the formation of Ni-O phase reconstructs on the surface of both materials. However, the increasement of the SRL on LD-NCM811 and NCM811 is different. From Supplementary **Fig. S17–18**, the ratio of $Ni^{2+}/(Ni^{2+} + Ni^{3+})$ of NCM811 and LD-NCM811 is 48.2% and 33.0% at 50th cycle respectively, and they increase to 61.3% and 39.0% at 100th cycle, suggesting more severer cation mixing of NCM811 than LD-NCM811. These results have unambiguously shown that cation mixing of LD-NCM811 is more trifling compared to NCM811 at the same sputtering time and the thickness of SRL of LD-NCM811 is thinner than NCM811 at the same cycle number. These findings are highly compliant with the TEM results and can explain the impedance spectrum and electrochemical performances. Injecting Li_2MnO_3 in NCM811 effectively suppresses the formation of SRL. When compared with the pristine sample, the XANES K-edge shifts to left after 100 cycles (Supplementary **Fig. S19**) of LD-NCM811, indicating the average valence state of nickel decreases. This can probably be explained by more Ni ions moving back to TM layer and less SRL blocking, which corroborates well with the subtle decay of discharge voltage. However, the average chemical state of Ni ions in NCM811 increases as the K-edge shift to right after cycling. Although the exact mechanism is unknown and needs further study, there are several possible reasons: 1) the thick SRL hinders the migration of Li^+, which results in some Li^+ unable to insert into Li layers in NCM811 during discharge, 2) less high valent Ni ions involve charge compensation when they occupy Li layer, and 3) the discharge voltage of NCM811 strays far from the equilibrium voltage due to the large polarization.

Fig. 5a,e exhibits the initial charge curve of LD-NCM811 and NCM811 on *in situ* XRD punch cell. Supplementary **Fig. S20** displays the XRD patterns of two electrodes in the *in situ* cell before electrochemical test. As shown in Fig. 5b, the (003) peak of LD-NCM811 gradually shifts to left and exhibits merely peak split in charge process. While for NCM811, the (003) peak shifts to the left at the beginning of the initial charging, then suddenly shifts to higher angle till the end of charging, which indicates NCM811 suffering from severe phase transition from H_2 to H_3. The corresponding crystal axis of *c* value increases until the voltage reaches to 3.9 V, followed by a sequential decline, as confirm by the Rietveld refinement of *c* lattice parameters in Fig. 5d, h. This can be possibly explained by the electrostatic repulsion predominant over the decrease in TM slab thickness at the initial deintercalation process when extraction of Li^+ from the lithium layers accompanying with oxidation of TM ions [70]. However, with further de-lithium state, Li^+ begins to extract from the TM slabs and TM ions of high state drawn more electrons from oxygen to TM-O bond, which causes electrostatic repulsion decreased between O slab, then lowers the c_{hex}. The contraction of c_{hex} above 4.2 V for LD-NCM811 and NCM811 is 1.14% and 1.62% respectively, indicating that injecting Li_2MnO_3 effectively maintains structural stability. As for a_{hex}, it relates to TM-TM ions and mainly declines from 3.7 to 3.9 V, resulting from oxidation of Ni^{3+} to Ni^{4+} [71]. The contraction of a_{hex} during charging process for LD-NCM811 and

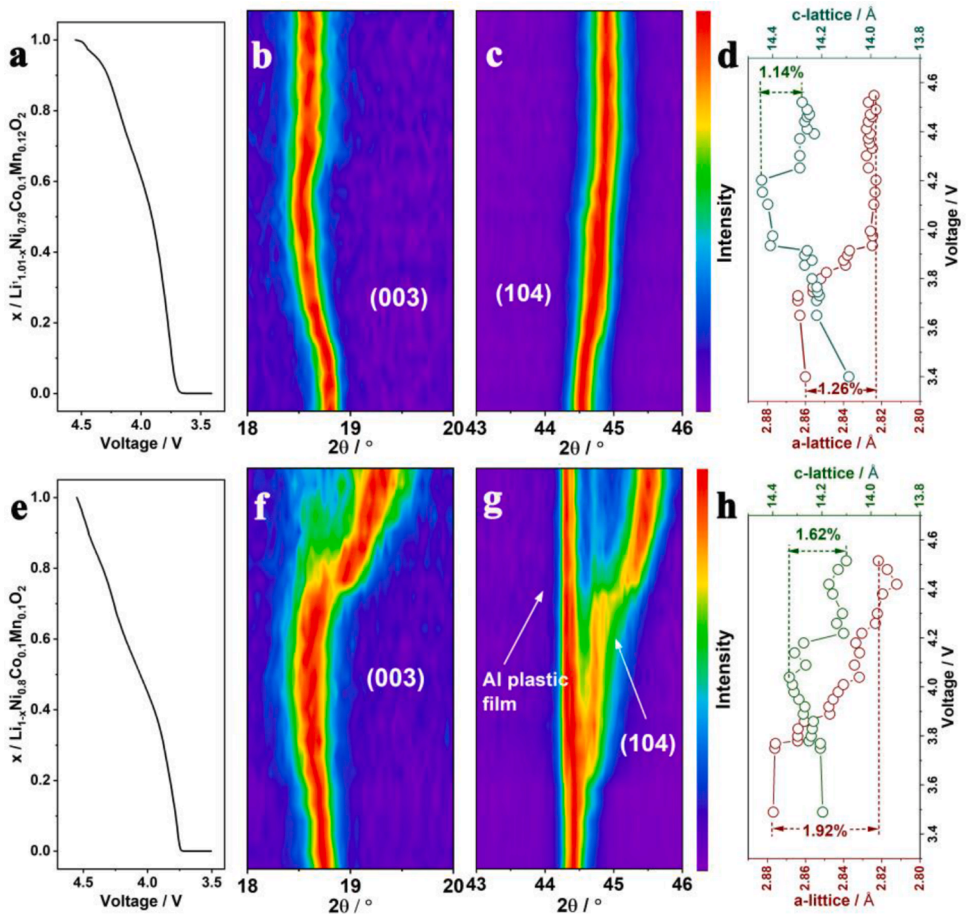

Fig. 5. *In situ* XRD of LD-NCM811 and NCM811 charged at 0.05 C rate between 2.8 and 4.55 V. The initial charge curve of LD-NCM811 (a) and NCM811 (e); (b-c, f-g) Contour plot of the diffraction patterns of (003) and (104) peaks in LD-NCM811 (b-c) and NCM811 (f-g); The evolutions of the lattice parameters *a* and *c* in LD-NCM811 (d) and NCM811 (h).

NCM811 is 1.26% and 1.92%, respectively, implying a significant role that Li_2MnO_3 plays in suppressing structural distortion. a_{hex} in LD-NCM811 stop decreasing at high voltage while charging continues, indicating that O^{2-}/O_2^{2-} redox pair begins to participate in charging process, confirming Li^+ de-lithium from TM layers [70]. I*n situ* XRD results reveal the extraction of Li^+ from TM layers to form lithium voids, suggesting the possibility of Ni ions migrating back to TM layers and *in situ* mitigating cation mixing.

Gibbs free energy of LD-NCM811 before/after *in situ* mitigating cation mixing is calculated by the projector-augmented wave method. According to Fig. 6a, Gibbs free energy of LD-NCM811 ($Li_3Ni_{25}Co_4Mn_4O_{72}$, stage 1) is −641.265 eV when LD-NCM811 is charged to 4.55 V. From stage 1 to stage 2, the Ni ion existing in lithium layer migrates to the adjacent tetrahedral structure passing through a coplanar. In this process, one Ni-O bond (Ni25-O8) is broken which increases the Gibbs free energy of the cell unit because breaking atomic bonds needs energy (stage 2). From stage 2 to stage 3, the Ni ion migrates into the adjacent tetrahedral structure and forms a Ni-O bond with another O ion (O3) which releases binding energy, decreasing the Gibbs free energy of the cell unit. In the next moment, the Ni ion (Ni25) forms a new Ni-O bond (Ni25-O8) with the O ion (O8) which is in the TM octahedral site (6c). In this stage (5), Gibbs free energy of LD-NCM811 is −641.859 eV, which is slightly lower than stage 3 because of formation of Ni25-O8 bond and lengthened other Ni-O bonds (Ni25-O2, Ni25-O9 and Ni25-O3, presented in Supplementary **Table S11**). Finally, the Ni ion continues to migrate in the octahedron in the TM layer breaking Ni25-O2 bond, passing through the coplanar between lithium and TM layer and forming new Ni-O bonds (Ni25-O2 (in the TM octahedral site (6c)) and Ni25-O4). Consequently, the Gibbs free energy decreases from −641.859 eV to −643.214 eV (stage 5–7). These calculation results show that Ni ions in lithium layers migrating back to TM layers is spontaneous with the help of Li_2MnO_3. Even if the Gibbs free energy may increase initially, the process is thermodynamically favorable, indicating the viability of *in situ* mitigating cation mixing as schematically illustrated in Fig. 6b. The feasibility of this work agrees with previous studies that Ni atoms are able to migrate to TM layers from Li layers spontaneously [72,73].

The DSC profiles of LD-NCM811 and NCM811 charged to 4.55 V is presented in Fig. 7a. NCM811 exhibites a large exothermic peak at 218 °C, whereas the exothermic peak of LD-NCM811 is 234 °C, 16 °C higher, and the onset temperature of LD-NCM811 also shifts 15 °C higher than NCM811. Fig. 7b shows minor capacity fade in LD-NCM811 with capacity retention of 93% after 100 cycles, whereas NCM811 retaining 75% of its initial capacity. These results indicate that injecting low content of Li_2MnO_3 into NCM811 at the cut-off voltage of 4.55 V improves the thermal stability of NCM811.

4. Conclusions

In this work, 2.38% Li_2MnO_3 is injected into NCM811 to form a high-performance LD-NCM811 cathode, with the Ni/Li mixing cation of LD-NCM811 distinctly suppressed from 13.5% to 7.5%. Compared to the conventional NCM811 cathode, the LD-NCM811 cathode exhibits improved capacity retention (93% after 200 cycles vs 68% for the NCM811 cathode), much enhanced structural and thermal stability. The enhanced electrochemical properties and battery performance are

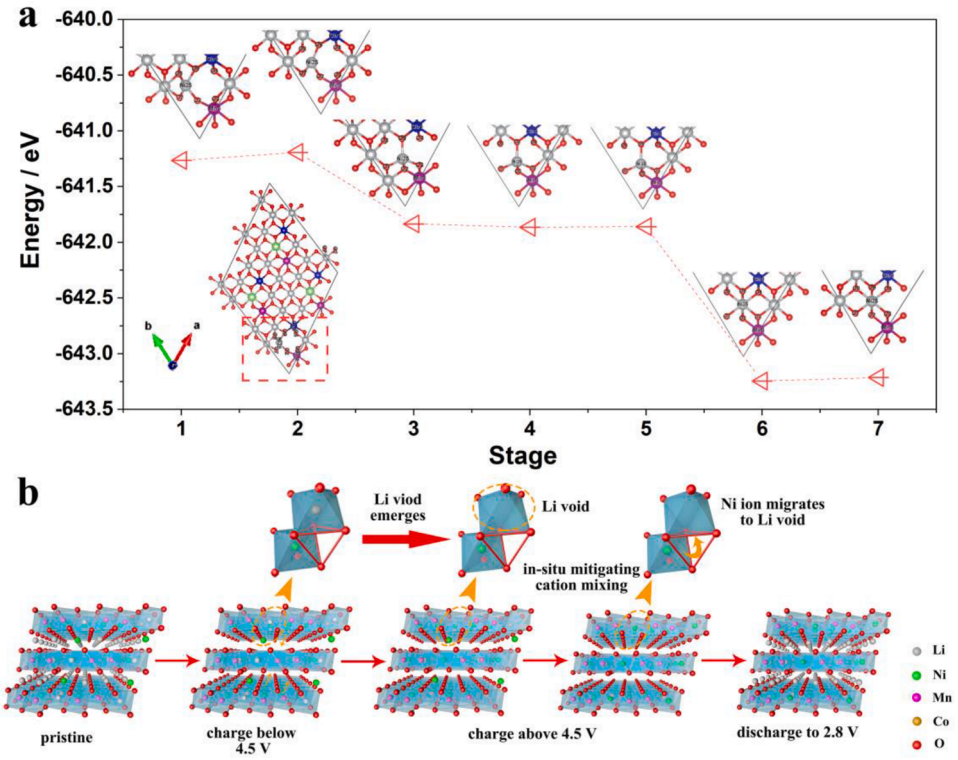

Fig. 6. The process of *in situ* mitigating cation mixing and their corresponding Gibbs free energy (a). Schematic diagram (b) of *in situ* mitigating cation mixing.

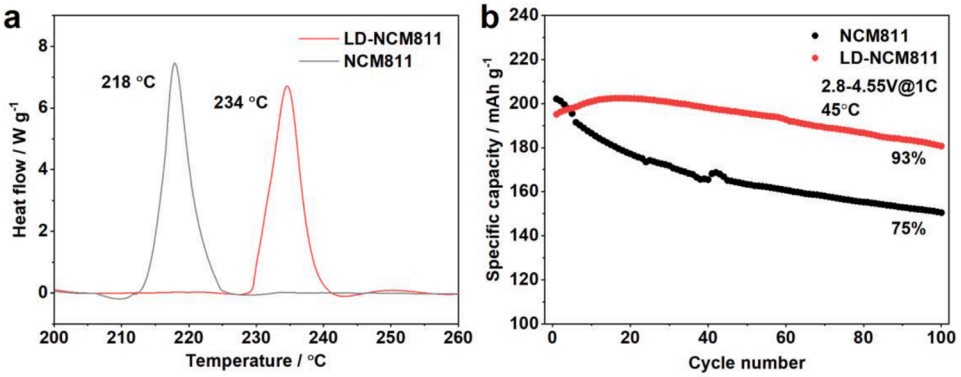

Fig. 7. DSC profiles (a) of the charged (4.55 V) LD-NCM811 and NCM811 cathodes measured at a scan rate of 10 °C min^{-1}. Cycling performance (b) of the LD-NCM811 and NCM811 cathodes at 1 C, 45 °C.

attributed to the presence of Li^+ in Li_2MnO_3 phase de-intercalation above 4.5 V and retaining lithium voids in TM layers. Such generated lithium voids are favorable for Ni^{2+} ions in lithium layers *in situ* migrating back to TM layers driven by thermodynamics, achieving mitigating cation mixing.

CRediT authorship contribution statement

Binhong Wu: Methodology, Investigation, Formal analysis, Visualization, Writing – original draft. **Zhiye Lin:** Investigation, Formal analysis. **Gaige Zhang:** Investigation, Formal analysis. **Dehui Zhang:** Investigation. **Wenguang Zhang:** Investigation. **Guanjie Li:** Investigation. **Yanxia Che:** Investigation. **Ling Chen:** Investigation. **Huirong Wang:** Investigation. **Weishan Li:** Resources, Supervision, Funding acquisition. **Min Chen:** Investigation, Software, Writing – review & editing, Validation, Funding acquisition. **Guozhong Cao:** Writing – review & editing, Conceptualization.

Declaration of Competing Interest

The authors declare that they have no competing financial interests or personal relationships.

Data availability

No data was used for the research described in the article.

Acknowledgment

This work is supported by National Natural Science Foundation of China (Grant No. 21872058 and No. 22109047), Foundation for Yong Teacher (Grant No. 20KJ20) and the Open Fund of Energy and Materials Chemistry Joint Laboratory of SCNU and TINCI (Grant No. SCNU-TINCI-2022).

Supplementary materials

Supplementary material associated with this article can be found, in the online version, at doi:10.1016/j.ensm.2022.09.008.

References

[1] J.B. Goodenough, Acc. Chem. Res. 46 (2013) 1053–1061.
[2] J.B. Goodenough, K.S. Park, J. Am. Chem. Soc. 135 (2013) 1167–1176.
[3] J.M. Zheng, S.J. Myeong, W.R. Cho, P.F. Yan, J. Xiao, C.M. Wang, J. Cho, J. G. Zhang, Adv. Energy Mater. 7 (2017), 1601284.
[4] F.X. Wu, G. Yushin, Energy Environ. Sci. 10 (2017) 435–459.
[5] A.K. Padhi, K.S. Nanjundaswamy, J.B. Goodenough, J. Electrochem. Soc. 144 (1997) 1188–1194.
[6] M.M. Thackeray, W.I.F. David, P.G. Bruce, J.B. Goodenough, Mater. Res. Bull. 18 (1983) 461–472.
[7] A. Chakraborty, S. Kunnikuruvan, S. Kumar, B. Markovsky, D. Aurbach, M. Dixit, D.T. Major, Chem. Mater. 32 (2020) 915–952.
[8] A. Manthiram, J.C. Knight, S.T. Myung, S.M. Oh, Y.K. Sun, Adv. Energy Mater. 6 (2016), 1501010.
[9] A. Manthiram, B.H. Song, W.D. Li, Energy Storage Mater. 6 (2017) 125–139.
[10] Y.K. Sun, ACS Energy Lett. 4 (2019) 1042–1044.
[11] S.T. Myung, F. Maglia, K.J. Park, C.S. Yoon, P. Lamp, S.J. Kim, Y.K. Sun, ACS Energy Lett. 2 (2017) 196–223.
[12] K.J. Park, J.Y. Hwang, H.H. Ryu, F. Maglia, S.J. Kim, P. Lamp, C.S. Yoon, Y.K. Sun, ACS Energy Lett. 4 (2019) 1394–1400.
[13] Y.K. Sun, S.T. Myung, M.H. Kim, J. Prakash, K. Amine, J. Am. Chem. Soc. 127 (2005) 13411–13418.
[14] Y.K. Sun, Z.H. Chen, H.J. Noh, D.J. Lee, H.G. Jung, Y. Ren, S. Wang, C.S. Yoon, S. T. Myung, K. Amine, Nat. Mater. 11 (2012) 942–947.
[15] Y.D. Xu, W. Xiang, Z.G. Wu, C.L. Xu, Y.C. Li, X.D. Guo, G.P. Lv, X. Peng, B. H. Zhong, Electrochim. Acta 268 (2018) 358–365.
[16] Q. Xie, W.D. Li, A. Manthiram, Chem. Mater. 31 (2019) 938–946.
[17] T. Weigel, F. Schipper, E.M. Erickson, F.A. Susai, B. Markovsky, D. Aurbach, ACS Energy Lett. 4 (2019) 508–516.
[18] R.K. Yang, Z.G. Wu, Y.C. Li, R. Li, L. Qiu, D. Wang, L. Yang, X.D. Guo, Ionics 26 (2020) 3223–3230.
[19] K.J. Park, M.J. Choi, F. Maglia, S.J. Kim, K.H. Kim, C.S. Yoon, Y.K. Sun, Adv. Energy Mater. 8 (2018), 1703612.
[20] L. Ni, R. Guo, S. Fang, J. Chen, J. Gao, Y. Mei, S. Zhang, W. Deng, G. Zou, H. Hou, X. Ji, eScience 2 (2022) 116–124.
[21] Y. Lu, Y.D. Zhang, Q. Zhang, F.Y. Cheng, J. Chen, Particuology 53 (2020) 1–11.
[22] X.M. Fan, G.R. Hu, B. Zhang, X. Ou, J.F. Zhang, W.G. Zhao, H.P. Jia, L.F. Zou, P. Li, Y. Yang, Nano Energy 70 (2020), 104450.
[23] H.H. Ryu, B. Namkoong, J.H. Kim, I. Belharouak, C.S. Yoon, Y.K. Sun, ACS Energy Lett. 6 (2021) 2726–2734.
[24] W. Gu, G. Xue, Q. Dong, R. Yi, Y. Mao, L. Zheng, H. Zhang, X. Fan, Y. Shen, L. Chen, eScience (2022), https://doi.org/10.1016/j.esci.2022.05.003.
[25] G. Kresse, J. Furthmuller, Phys. Rev. B 54 (1996) 11169–11186.
[26] J.P. Perdew, K. Burke, M. Ernzerhof, Phys. Rev. Lett. 77 (1996) 3865–3868.
[27] V.I. Anisimov, F. Aryasetiawan, A.I. Lichtenstein, J. Phys. Condens. Matter 9 (1997) 767–808.
[28] S.H. Park, K.S. Park, Y.K. Sun, K.S. Nahm, Y.S. Lee, M. Yoshio, Electrochim. Acta 46 (2001) 1215–1222.
[29] J.C. Zheng, Z. Yang, A. Dai, L.B. Tang, H.X. Wei, Y.J. Li, Z.J. He, J. Lu, Small 15 (2019), 1904854.
[30] C.C. Fu, G.S. Li, D. Luo, Q. Li, J.M. Fan, L.P. Li, ACS Appl. Mater. Interfaces 6 (2014) 15822–15831.
[31] Q.L. Wu, V.A. Maroni, D.J. Gosztola, D.J. Miller, D.W. Dees, W.Q. Lu, J. Electrochem. Soc. 162 (2015) A1255–A1264.
[32] M. Chen, D. Chen, Y. Liao, X. Zhong, W. Li, Y. Zhang, ACS Appl. Mater. Interfaces 8 (2016) 4575–4584.
[33] G. Sun, F.D. Yu, L.F. Que, L. Deng, M.J. Wang, Y.S. Jiang, G.J. Shao, Z.B. Wang, Nano Energy 66 (2019), 104102.
[34] J. Yang, Y. Xia, ACS Appl. Mater. Interfaces 8 (2016) 1297–1308.
[35] J. Kim, H. Cho, H.Y. Jeong, H. Ma, J. Lee, J. Hwang, M. Park, J. Cho, Adv. Energy Mater. 7 (2017), 1602559.
[36] L. Qiu, W. Xiang, W. Tian, C.L. Xu, Y.C. Li, Z.G. Wu, T.R. Chen, K. Jia, D. Wang, F. R. He, X.D. Guo, Nano Energy 63 (2019), 103818.
[37] A. Boulineau, L. Croguennec, C. Delmas, F. Weill, Chem. Mater. 21 (2009) 4216–4222.
[38] S.W. Lee, H. Kim, M.S. Kim, H.C. Youn, K. Kang, B.W. Cho, K.C. Roh, K.B. Kim, J. Power Sources 315 (2016) 261–268.
[39] J.R. Croy, J.S. Park, F. Dogan, C.S. Johnson, B. Key, M. Balasubramanian, Chem. Mater. 26 (2014) 7091–7098.
[40] A.R. Armstrong, M. Holzapfel, P. Novak, C.S. Johnson, S.H. Kang, M.M. Thackeray, P.G. Bruce, J. Am. Chem. Soc. 128 (2006) 8694–8698.
[41] H.D. Liu, Y. Chen, S. Hy, K. An, S. Venkatachalam, D.N. Qian, M.H. Zhang, Y. S. Meng, Adv. Energy Mater. 6 (2016), 1502143.
[42] N. Yabuuchi, K. Yoshii, S.T. Myung, I. Nakai, S. Komaba, J. Am. Chem. Soc. 133 (2011) 4404–4419.
[43] Q.Y. Lin, W.H. Guan, J. Meng, W. Huang, X. Wei, Y.W. Zeng, J.X. Li, Z. Zhang, Nano Energy 54 (2018) 313–321.
[44] X. Xiong, Z. Wang, G. Yan, H. Guo, X. Li, J. Power Sources 245 (2014) 183–193.
[45] S.G. Woo, J.H. Han, K.J. Kim, J.H. Kim, J.S. Yu, Y.J. Kim, Electrochim. Acta 153 (2015) 115–121.
[46] Y. Jiang, Y.J. Bi, M. Liu, Z. Peng, L.Y. Huai, P. Dong, J.G. Duan, Z.L. Chen, X. Li, D. Y. Wang, Y.J. Zhang, Electrochim. Acta 268 (2018) 41–48.
[47] D. Becker, M. Borner, R. Nolle, M. Diehl, S. Klein, U. Rodehorst, R. Schmuch, M. Winter, T. Placke, ACS Appl. Mater. Interfaces 11 (2019) 18404–18414.
[48] Q.M. Gan, N. Qin, Y.H. Zhu, Z.X. Huang, F.C. Zhang, S. Gu, J.W. Xie, K.L. Zhang, L. Lu, Z.G. Lu, ACS Appl. Mater. Interfaces 11 (2019) 12594–12604.
[49] S.D. Yang, Q.L. Fan, Z.C. Shi, L.Y. Liu, J. Liu, X. Ke, J.P. Liu, C.Y. Hong, Y. Yang, Z. P. Guo, ACS Appl. Mater. Interfaces 11 (2019) 36742–36750.
[50] Y.P. Jiang, Z.H. Liu, Y.Z. Zhang, H.L. Hu, X.G. Teng, D.L. Wang, P. Gao, Y.M. Zhu, Electrochim. Acta 309 (2019) 74–85.
[51] Q.L. Fan, S.D. Yang, J. Liu, H.D. Liu, K.J. Lin, R. Liu, C.Y. Hong, L.Y. Liu, Y. Chen, K. An, P. Liu, Z.C. Shi, Y. Yang, J. Power Sources 421 (2019) 91–99.
[52] Z. Feng, R. Rajagopalan, D. Sun, Y.G. Tang, H.Y. Wang, Chem. Eng. J. 382 (2020), 122959.
[53] Q.W. Ran, H.Y. Zhao, Y.Z. Hu, S. Hao, Q.Q. Shen, J.T. Liu, H. Li, Y. Xiao, L. Li, L. P. Wang, X.Q. Liu, ACS Appl. Mater. Interfaces 12 (2020) 9268–9276.
[54] J. Li, M.L. Zhang, D.Y. Zhang, Y.X. Yan, Z.M. Li, Chem. Eng. J. 402 (2020), 126195.
[55] W.H. Zhang, L.W. Liang, F. Zhao, Y. Liu, L.R. Hou, C.Z. Yuan, Electrochim. Acta 340 (2020), 135871.
[56] F. Zhang, K.M. Wu, L.J. Zhang, X. Hu, K.F. Yu, C. Liang, W.M. Jin, Ionics 27 (2021) 2367–2380.
[57] M.A.R. Khollari, M.K. Azar, M. Esmaeili, N. Malekpour, S.M. Hosseini-Hosseinabad, R.S. Moakhar, A. Dolati, S. Ramakrishna, ACS Appl. Energy Mater. 4 (2021) 5304–5315.
[58] L. You, B. Chu, G. Li, T. Huang, A. Yu, J. Power Sources 482 (2021), 228940.
[59] J.L. Tao, A.N. Mu, S.J. Geng, H. Xiao, L.T. Zhang, Q.S. Huang, J. Solid State Electrochem. 25 (2021) 1959–1974.
[60] G.J. Li, Y.H. Liao, Z.F. Li, N. Xu, Y.K. Lu, G.Y. Lan, G.Z. Sun, W.S. Li, ACS Appl. Mater. Interfaces 12 (2020) 37013–37026.
[61] J.M. Zheng, P.F. Yan, L. Estevez, C.M. Wang, J.G. Zhang, Nano Energy 49 (2018) 538–548.
[62] Y.S. Meng, G. Ceder, C.P. Grey, W.S. Yoon, M. Jiang, J. Breger, Y. Shao-Horn, Chem. Mater. 17 (2005) 2386–2394.
[63] L. Xiao, J. Xiao, X.Q. Yu, P.F. Yan, J.M. Zheng, M. Engelhard, P. Bhattacharya, C. M. Wang, X.Q. Yang, J.G. Zhang, Nano Energy 16 (2015) 143–151.
[64] A. Boulineau, L. Simonin, J.F. Colin, E. Canevet, L. Daniel, S. Patoux, Chem. Mater. 24 (2012) 3558–3566.
[65] J. Bareno, C.H. Lei, J.G. Wen, S.H. Kang, I. Petrov, D.P. Abraham, Adv. Mater. 22 (2010) 1122–1127.
[66] H.L. Zhang, F. Omenya, P.F. Yan, L.L. Luo, M.S. Whittingham, C.M. Wang, G. W. Zhou, ACS Energy Lett. 2 (2017) 2607–2615.
[67] D.P. Abraham, R.D. Twesten, M. Balasubramanian, I. Petrov, J. McBreen, K. Amine, Electrochem. Commun. 4 (2002) 620–625.
[68] Y. Makimura, S.J. Zheng, Y. Ikuhara, Y. Ukyo, J. Electrochem. Soc. 159 (2012) A1070–A1073.
[69] J.L. Shi, J.N. Zhang, M. He, X.D. Zhang, Y.X. Yin, H. Li, Y.G. Guo, L. Gu, L.J. Wan, ACS Appl. Mater. Interfaces 8 (2016) 20138–20146.
[70] Z.H. Lu, J.R. Dahn, J. Electrochem. Soc. 149 (2002) A815–A822.
[71] X. Li, Y. Qiao, S.H. Guo, Z.M. Xu, H. Zhu, X.Y. Zhang, Y. Yuan, P. He, M. Ishida, H. S. Zhou, Adv. Mater. 30 (2018), 1705197.
[72] M.Y. Yang, S. Kim, K. Kim, W. Cho, J.W. Choi, Y.S. Nam, Adv. Funct. Mater. 27 (2017), 1700982.
[73] S. Kim, W. Cho, X. Zhang, Y. Oshima, J.W. Choi, Nat. Commun. 7 (2016) 13598.